Applied Physics B (2023) 129:56
https://doi.org/10.1007/s00340-023-07996-y

Applied Physics B
Lasers and Optics

RESEARCH

Characteristics of electron beams accelerated by parallel and antiparallel circularly polarized Laguerre–Gaussian laser pulses

Hoon Song[1,2] · Ki Hong Pae[1,3] · Junho Won[1,2] · Jaehyun Song[1,2] · Seongmin Lee[1,2] · Chul Min Kim[1,3] · Chang-Mo Ryu[1] · Woosuk Bang[1,2] · Chang Hee Nam[1,2]

Received: 31 May 2022 / Accepted: 5 March 2023 / Published online: 24 March 2023

Abstract
A direct comparison of the properties of electron beam generated by antiparallel circularly polarized Laguerre–Gaussian (CPLG) laser pulse and parallel CPLG laser pulse has been performed with three-dimensional particle-in-cell simulations. It is known that the longitudinal field of an antiparallel CPLG laser pulse with opposite signs of spin and orbital quantum number preferentially accelerates electrons to high energy. However, a direct comparison of electron beam between the other combination of spin and orbital angular momentum, the parallel CPLG laser pulse with the same sign of spin and orbital angular quantum number, has not been conducted. While the two pulses have an identical transverse field envelope, the generated electron beam properties are different. Although the magnitude of the longitudinal field is about one order of magnitude less than that of the transverse field, it has a significant effect on beam divergence. For antiparallel CPLG laser pulse, collimated electron bunches are formed with small divergence (< 50 mrad); while for parallel CPLG laser pulse, a diverging (> 100 mrad) electron beam is formed. This difference in beam quality can indicate a field-induced acceleration in actual experiments. A few-cycle laser pulse and low-density plasma are used to rule out the effect of laser–plasma interaction. It is also shown that for antiparallel CPLG laser pulse, the maximum kinetic energy increases with the square root of incident laser power, consistent with the scaling law for field-induced acceleration.

1 Introduction

For more than two decades, efforts have been made to accelerate charged particles using ultra-intense lasers [1–6], as laser technology advances at a rapid pace [7]. Laser-driven charged particle accelerations have a wide range of applications, from medical to fundamental research [8–13]. Currently, the majority of laser particle acceleration schemes rely on the plasma field induced by high-intensity laser pulses [2, 9]. A typical example is the target normal sheath acceleration mechanism, in which protons are accelerated to near 100 MeV by the plasma sheath field generated by a high-intensity laser pulse [14, 15]. For the acceleration of electrons to multi-GeV, the laser wakefield acceleration (LWFA) mechanism is used, which makes use of the wakefield generated by a laser pulse propagating through a plasma [16–19].

As an alternative to these schemes based on laser-induced plasma fields, a scheme that accelerates electrons directly with the field of the laser pulse, called the vacuum laser acceleration (VLA) scheme, has recently gained attention [20–24]. Usually, the scheme uses a radially polarized laser pulse that has a strong longitudinal electric field near the optical axis [25–30]. As the transverse electric field of such a pulse has radial components only, the accelerated electrons have a smaller emittance compared with those accelerated by a usual linearly polarized pulse. However, an ultra-intense radially polarized laser pulse is very difficult to produce because the polarization converter should be able to assign the polarization angles as a function of the incident laser pulse's azimuthal angle [25, 31].

On the other hand, several VLA electron scenarios using CPLG laser pulse have been proposed. In fact, a mirror-type

✉ Woosuk Bang
wbang@gist.ac.kr

Chul Min Kim
chulmin@gist.ac.kr

1 Center for Relativistic Laser Science, Institute for Basic Science (IBS), Gwangju 61005, Korea

2 Department of Physics and Photon Science, Gwangju Institute of Science and Technology, Gwangju 61005, Korea

3 Advanced Photonics Research Institute, Gwangju Institute of Science and Technology, Gwangju 61005, Korea

phase plate has been developed recently as a practical way to produce ultra-intense CPLG laser pulses [32]. The CPLG laser pulse is a laser pulse that has an orbital angular momentum (OAM), l, in addition to the linear momentum, and the spin angular momentum (SAM), $s = \pm 1$, or the polarization of light [33]. In previous studies [34–38], the antiparallel $((l = +1, s = -1), (l = -1, s = +1))$ CPLG laser pulses have been used for CPLG VLA electron beam generation. An antiparallel CPLG pulse has characteristics that the longitudinal field is distributed on the optical axis. Using these characteristics on the longitudinal field, a high-density attosecond electron bunch is created by the interaction of nano-fiber and micro-droplets interacting with intense antiparallel CPLG laser pulses [34, 35]. In addition, a method using a plasma mirror has been suggested [36]. This method uses the reflection of the antiparallel CPLG laser pulse from a plasma mirror which simultaneously injects copious electrons from the plasma mirror and directly accelerates the injected electrons. According to their simulation results, they expect a 0.47 GeV electron beam using a 0.6 PW antiparallel CPLG laser pulse and plasma mirror. The trapping effect of the longitudinal magnetic field as well as the acceleration effect of the longitudinal electric field during the electron acceleration processes were analyzed in detail [37]. In the most recent study, the evidence of direct field-induced acceleration was presented by confirming the carrier-envelope-phase dependence of electron acceleration using a few-cycle antiparallel CPLG laser pulse [38].

We compare an electron beam generated by a parallel CPLG laser pulse $(l = +1, s = +1)$ to that produced by an antiparallel CPLG laser pulse. The parallel CPLG laser pulse has an identical transverse field envelope while having a completely different longitudinal field structure. Although it was mentioned in [38] that the parallel CPLG laser pulses cannot accelerate electrons, the distinction between the generated electron beams was not examined. However, the electron beams created by two distinct laser pulses can be the experimental indicator for direct field-induced acceleration. In addition, we investigate the interaction of low-density plasmas with CPLG laser pulses. This examines the difference in electron beams caused by laser–particle interaction while excluding the laser–plasma effect.

2 Field structure of a Laguerre–Gaussian laser mode

In this section, we express the longitudinal field of the CPLG laser mode using the paraxial approximation. Then, the solution to the Helmholtz equation is the Laguerre–Gaussian (LG) laser mode in the cylindrical coordinates (r, θ, z), and the wavefunction of the LG laser mode, $u_{l,p}$, can be written as

$$u_{l,p}(r,\theta,z) = A_a a_{norm} \left(\frac{w_0}{w(z)}\right)\left(\frac{\sqrt{2}r}{w(z)}\right)^{|l|} e^{-\frac{r^2}{w(z)^2}} L_p^{|l|}\left(\frac{2r^2}{w(z)^2}\right) \exp\left(i(\phi - l\theta)\right), \tag{1}$$

where l is the azimuthal index having an integer value, non-negative p is the radial index, A_a is the maximum wave amplitude, $a_{norm} = (e/|l|)^{|l|/2}$ is a normalization factor, $w(z) = w_0\sqrt{1 + \left(z/z_R\right)^2}$ is the beam radius, w_0 is the waist radius, $z_R = kw_0^2/2$ is the Rayleigh length, $L_p^{|l|}$ is the Laguerre polynomial, $\phi = -kz - kr^2/2R(z) + (|l| + 2p + 1)\Phi_G - \theta_0$ is the phase, $R(z) = z\left(1 + \left(z_R/z\right)^2\right)$ is the radius of curvature, $\Phi_G = \tan^{-1}\left(z/z_R\right)$ is the Gouy phase, $k = 2\pi/\lambda$ is the wavenumber, λ is the wavelength, and θ_0 is the offset phase. For simplicity, we only consider $l = \pm 1$ and the zeroth mode $p = 0$, i.e., $L_{p=0}^{|l|} = 1$.

For finding the longitudinal electric field of a CPLG laser mode, we start with a complex vector potential in the Coulomb gauge where the electric potential V is 0. In the paraxial approximation, the complex vector potential $\boldsymbol{A}$ of a circularly polarized laser mode is written as $\boldsymbol{A} = \left(A_x, -isA_x, -i/k\left(\partial_x A_x - is\partial_y A_x\right)\right)\exp(i\omega t)/\sqrt{2}$, where s is the SAM of photon and can have either + 1 (left circular polarization) or -1 (right circular polarization). Substituting A_x with the solution to Helmholtz equation $u_{l,p=0}$ and using Faraday's law of induction, $\boldsymbol{E} = -\partial_t \boldsymbol{A}$, the real components of the electric field of a CPLG laser mode are

$$\begin{pmatrix} E_x \\ E_y \end{pmatrix} = E_0 a_{norm}\left(\frac{w_0}{w(z)}\right)\left(\frac{\sqrt{2}r}{w(z)}\right)^{|l|} e^{-\frac{r^2}{w(z)^2}} \frac{1}{\sqrt{2}} \begin{pmatrix} \sin(\omega t + \phi - l\theta) \\ -s\cos(\omega t + \phi - l\theta) \end{pmatrix}, \tag{2}$$

$$E_z = E_0 a_{norm}\left(\frac{w_0}{w(z)}\right)\left(\frac{\sqrt{2}r}{w(z)}\right)^{|l|-1} e^{-\frac{r^2}{w(z)^2}} \frac{1}{kw(z)} \times \left((s\cdot l - |l|)\cos(\omega t + \phi - (l+s)\theta) + \frac{2r^2}{w_0^2}\cos\left(\omega t + \phi - (l+s)\theta + \Phi_G\right)\right), \tag{3}$$

where the maximum transverse electric field strength $E_{T,Max}$ in Eq. (2) is $E_0/\sqrt{2}$, not E_0. This convention is chosen to ensure that the time-averaged intensity is identical to the case of a linearly polarized laser mode. Note that the normalized transverse field amplitude is defined as $a_0 = E_0(mc\omega/e)^{-1}$ in this convention. Likewise, we normalize the longitudinal field amplitude as $a_{z0} = E_{z,\mathrm{Max}}(mc\omega/e)^{-1}$, where $E_{z,Max}$ is the maximum longitudinal electric field strength.

The longitudinal electric field, E_z, of a CPLG laser mode in Eq. (3) has three important properties. First, the longitudinal field contains the term of a total angular momentum times azimuthal phase dependence, $(l+s)\theta$. Since the polarization of the light can be either $s=+1$ or $s=-1$, the longitudinal field wavefront becomes planar only when $(l=-1, s=+1)$ or $(l=+1, s=-1)$. Figure 1a shows the normalized longitudinal electric field in the xy plane at the focus for the case $(l=-1, s=+1)$, while Fig. 1b shows the case of $(l=+1, s=+1)$ for comparison. When l is − 1, the longitudinal electric field $E_z(l=-1, s=+1)$ has no angular dependence since $(-1+1)\,\theta=0\,\theta$ and results in a large field along the propagation direction. Figure 1a shows this field structure on the focal plane, which offers the opportunity of an efficient electron acceleration along the z direction. On the other hand, when l is + 1, the longitudinal electric field $E_z(l=+1, s=+1)$ has phase dependence of $(1+1)\theta=2\theta$, and we do not expect an efficient electron acceleration because the laser pulse cannot keep the accelerated electrons in the same phase.

Second, in the expression for E_z in Eq. (3), there is a spin–orbit coupling term, $(s\cdot l-|l|)$, which vanishes when the orbital and spin quantum numbers have the same signs, dubbed as the "parallel" case. On the other hand, the term becomes $-2|l|$ when the orbital and spin quantum numbers have different signs, which we call the "antiparallel" case. In the antiparallel case, the longitudinal field is proportional to $E_z \propto -2|l|r^{|l|-1}\exp(-r^2/w_0^2)$ when $r \ll w_0$. In Fig. 1a, where l is − 1 and s is + 1, the longitudinal field is strong around the optical axis because $E_z \propto -2\exp(-r^2/w_0^2)$. In contrast, the longitudinal electric field vanishes around the optical axis in Fig. 1b because $E_z \propto r^2\exp(-r^2/w_0^2)$ when both l and s are + 1. An intuitive geometrical argument is given on the spin–orbit nature of the longitudinal electric field of the CPLG laser mode in Ref. 40.

Third, the maximum longitudinal electric field $E_{z,\mathrm{Max}}$ is $2\sqrt{2e}/kw_0 \times E_{T,\mathrm{Max}}$ on the focal plane in the antiparallel case. For example, when the laser wavelength is 800 nm, and the waist radius w_0 is 3 µm, $2\sqrt{2e}/kw_0$ is about 1/5. To accelerate electrons to relativistic speed with the longitudinal electric field, the normalized longitudinal field amplitude $a_{z0} = E_{z,\mathrm{Max}} \times (mc\omega/e)^{-1}$ should be larger than 1. Then, the normalized transverse field amplitude should satisfy $a_0 = E_0 \cdot (mc\omega/e)^{-1} > 5\sqrt{2}$. Note that the transverse field strength $|E_T|$ has the same donut shape for both antiparallel and parallel cases, as shown in Fig. 1c. In Fig. 1c, d, the transverse field strength is reduced by

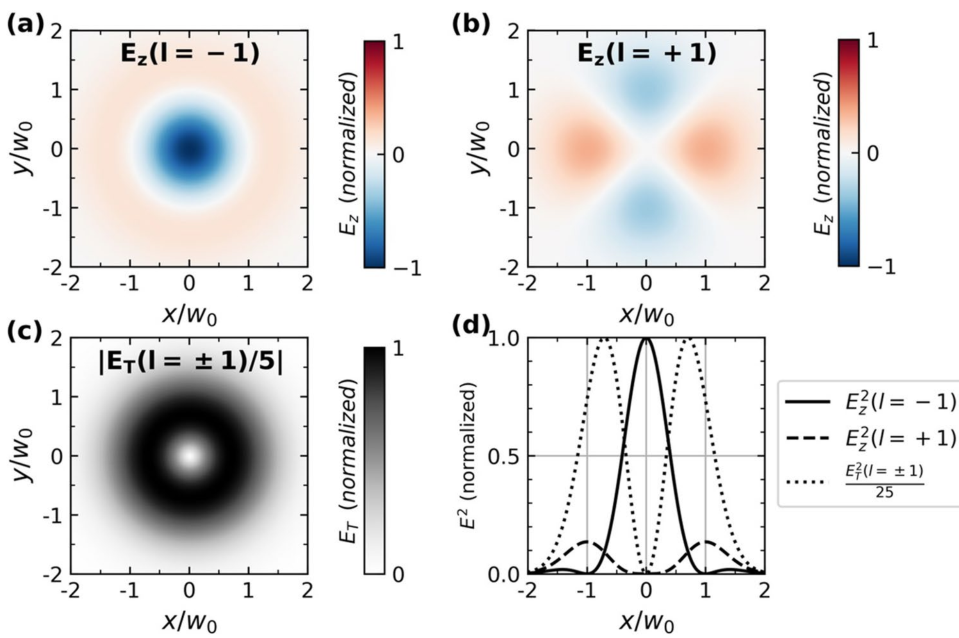

Fig. 1 Field structures of CPLG laser modes. **a** The longitudinal field amplitudes on the focal plane for the antiparallel case, $E_z(l=-1, s=+1)$. **b** The longitudinal field amplitude for the parallel case, $E_z(l=+1, s=+1)$. **c** The transverse field strength for both l, $|E_T(l=\pm1, s=+1)| = \sqrt{E_x^2+E_y^2}$. Transverse field strength is multiplied by $2\sqrt{2e}/kw_0$=1/5, which corresponds to kw_0 of 24. **d** The square of the longitudinal field strength in the antiparallel case (solid). The square of the longitudinal field strength in the parallel case (dashed). The square of the transverse field strength multiplied by $\left(2\sqrt{2e}/kw_0\right)^2 = 1/25$ is shown as a dotted line. All fields are normalized to the maximum longitudinal field strength in the antiparallel case, $E_z\left(l=-1, \sigma_z=+1\right)(r=0, z=0)$. The x and y axes are normalized to the waist radius, w_0

a factor of $2\sqrt{2e}/kw_0 = 1/5$, and is normalized to the maximum longitudinal electric field for $l = -1$ case. The solid line in Fig. 1d represents the square of the longitudinal field strength on the x-axis for the antiparallel case, i.e., $E_z^2(l = -1)$. As expected, the square of the longitudinal field strength shows a maximum at $x = 0$. The dashed line in Fig. 1d represents $E_z^2(l = +1)$, which presents much smaller peaks at $x/w_0 = \pm 1$. The dotted line in Fig. 1d indicates the square of the normalized transverse field strength, which peaks at $x/w_0 = \pm 1/\sqrt{2}$. An LG laser pulse with a relativistic transverse electric field $a_0 > 1$ pushes electrons inward as well as outward owing to the ponderomotive force. In our VLA scenario, an electron pushed inward is accelerated by the longitudinal electric field near the optical axis if it is antiparallel.

3 Results and discussion

The electron acceleration by the longitudinal field of the antiparallel and parallel CPLG laser pulses are examined, using a fully relativistic particle-in-cell code, EPOCH3D [39]. The simulation box has dimensions of $80 \times 80 \times 15\,\mu\text{m}^3$ and is divided into $480 \times 480 \times 375$ cells. The initial plasma is located within the Rayleigh range, $0 < z < z_R$. For both electrons and protons, 30 computational particles per species are assigned to each cell, corresponding to a total of 2×10^9 computational particles for each species. The number density is identically set to have $10^{-5} n_c$ for both particle species. The density of the plasma was set so low to avoid the action of the plasma fields in the acceleration. Since plasma phenomenon is not involved in our simulation settings, a cell size of $\lambda/20$ in the longitudinal direction results in sufficient resolution for the electron acceleration process. We consider 800 nm laser pulses with a spot size of 2.0 μm in full width at half maximum (FWHM), which corresponds to $kw_0 = 13$. In this spot size, the paraxial approximation, $kw_0 \gg 1$, remains valid. A short laser pulse having a 5-fs pulse duration (FWHM) is employed so that electrons can experience the strongest longitudinal electric field. If the pulse duration is much longer than this, electrons do not experience the strongest longitudinal electric field because they are pushed away at the leading edge of the pulse where $a_{z0} \approx 1$. Under these circumstances, one should use a plasma mirror [40] or a pin-hole mirror [41] to inject pre-accelerated electrons into the peak of the laser pulse. We have used a 2 PW laser pulse to obtain the main data. The SAM of the laser pulse is fixed to the left circular polarization, or $s = +1$, in our simulations. After the pulse is gone ($t = 11$ fs), the simulation window follows the accelerated electrons moving at the speed of light.

Figure 2a, b illustrates the electron distribution along with the longitudinal electric field distribution in the xz plane at 125 fs. The two pulses have identical transverse field envelopes, resulting in the same ponderomotive force on the electrons. However, due to the different longitudinal field

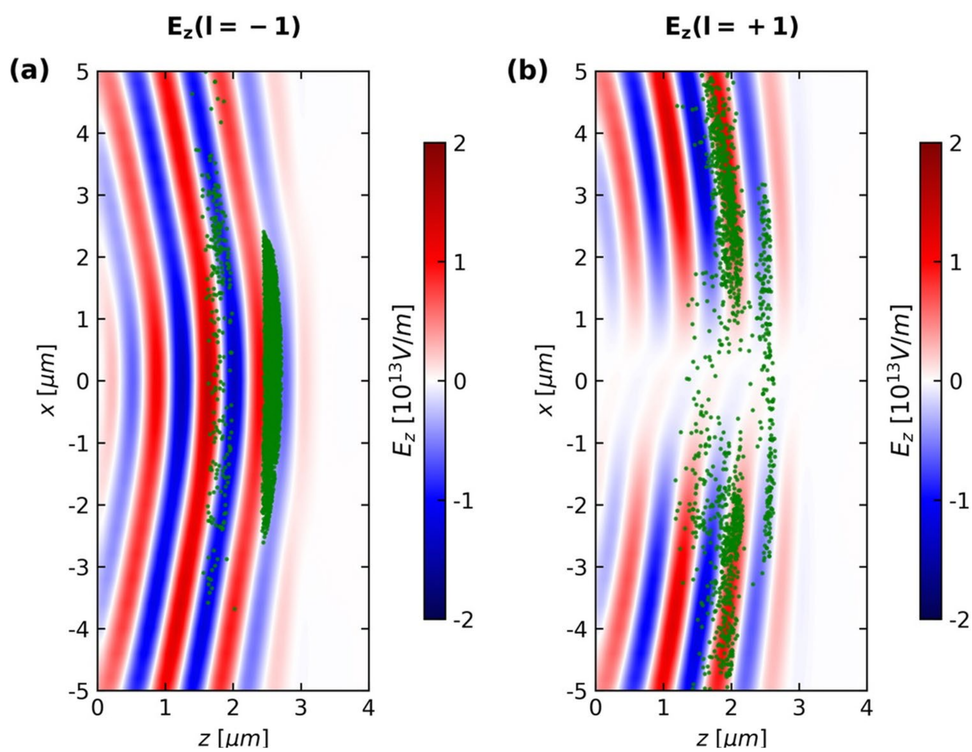

Fig. 2 Distributions of electrons (green dots) and longitudinal electric fields (background color). **a** In the antiparallel case, the majority of electrons are trapped by the longitudinal field around the optical axis. **b** In the parallel case, the longitudinal field is 0 V/m around the optical axis. In both figures, electrons with kinetic energy greater than 200 MeV are shown at a simulation time of 125 fs. In these simulations, a 2 PW laser power has been used

structures, the distributions of electrons are different. For the antiparallel case, trapped electron bunches are present as well as a strong longitudinal electric field around the optical axis. In contrast, Fig. 2b shows no longitudinal electric field around the optical axis, and the accelerated electrons spread out more.

For the quantitative analysis of the electron beam divergence, accelerated electrons are plotted in the *xy* plane in Fig. 3. The divergence of a electron θ is calulcated by $\sqrt{v_x^2 + v_y^2}/|v_z|$, and calculated divergence is indicated with a color code at the position of electrons' position. In the antiparallel case of Fig. 3a, the electron beam shows less spread. In the parallel case of Fig. 3b, the electron beam divergence is much more pronounced. There are two factors contributing to the observed differences in electron divergence between these two cases. First, the antiparallel and parallel CPLG laser pulses have the same transverse envelope but different field structure, which can affect the electron distribution and divergence. Second, the different longitudinal field structures in the two cases also play an important role in the observed divergence differences. Our analysis suggests that the transverse field has a minimal impact on the divergence distribution, and that the longitudinal field is the primary cause of the divergence differences observed in Fig. 3. (See Supplementary Fig. S1 for details.) Besides the beam divergence, the beam emittance is also an important parameter for the beam quality. Therefore, we have calculated the geometric emittance of the electron beams for both cases. In Fig. 3a, the electron beam radius is $< \Delta r > \approx 9.8$ μm and the beam divergence is $< \theta > \approx 54.6$ mrad. This results in a geometric beam emittance of 0.54 mm•mrad for the antiparallel case. In comparison, the electron beam radius is $< \Delta r > \approx 17.6$ μm and the beam divergence is $< \theta > \approx 117.9$ mrad in Fig. 3b. This results in a beam emittance of 2.07 mm•mrad for the parallel case, which is about four times larger than that in the antiparallel case. This result shows that an antiparallel CPLG laser pulse is a better electron beam driver than a parallel CPLG laser pulse.

The normalized energy spectra of accelerated electrons for both antiparallel and parallel cases are shown in Fig. 4a. The solid black line indicates the energy spectrum for the antiparallel case, and the dashed black line shows that for the parallel case. The figure clearly shows that the antiparallel CPLG laser pulse produces more high-energy electrons than the parallel CPLG laser pulse. We find that the antiparallel

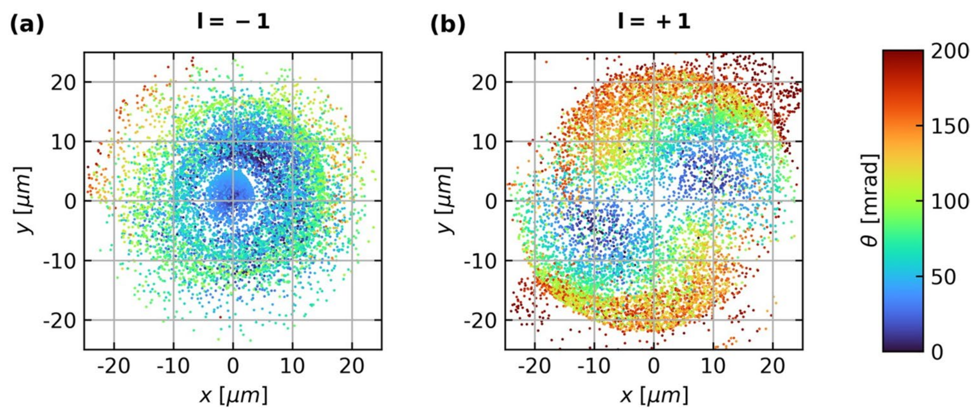

Fig. 3 Divergence distribution of electrons. **a** In the antiparallel case, most of the electrons have divergences less than 50 mrad. **b** In the parallel case, the electron beam divergence exceeds 100 mrad. Electrons with kinetic energy greater than 200 MeV are shown at a simulation time of 600 fs. In these simulations, $P = 2$ PW is used

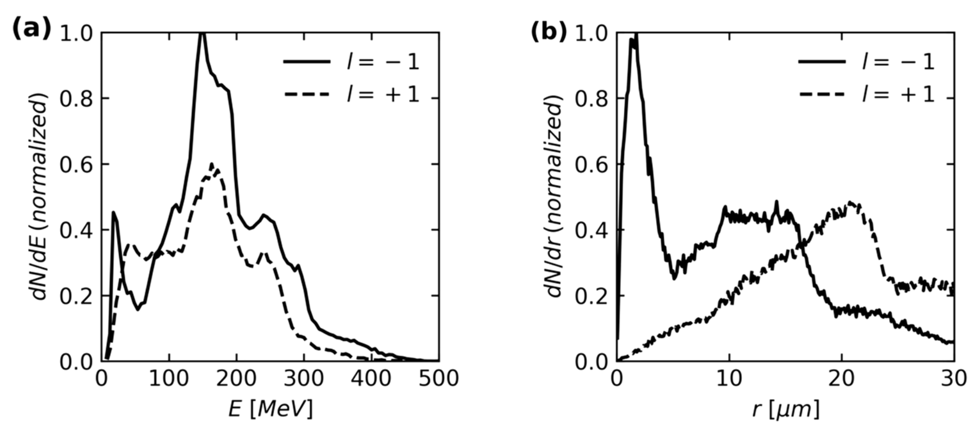

Fig. 4 Energy spectrum and radial distribution of electrons. **a** Normalized energy spectra of the accelerated electrons are shown in this plot. **b** Normalized radial distributions of electrons are shown for both $l = -1$ and $l = +1$. The solid black line indicates the distribution in the antiparallel case. The dashed black line represents the distribution in the parallel case. In these simulations, $P = 2$ PW is used. The simulation time is 600 fs

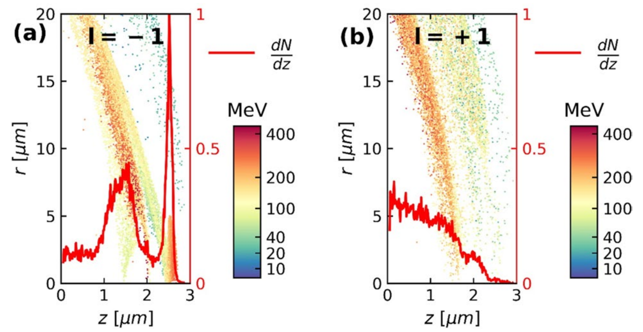

Fig. 5 **a** Normalized longitudinal number density (solid red line) of the accelerated electrons for the antiparallel case. Background dots represent the distribution of the accelerated electrons in the (r, z) plane. Color code represents the energy of each electron. **b** A similar figure is drawn for the parallel case. For the longitudinal number density, both figures are normalized to the peak electron density in **a**. In these simulations, $P = 2$ PW is used. The simulation time is 600 fs

CPLG laser pulse produces 42% more electrons with energy above 100 MeV than the parallel CPLG laser pulse. Figure 4b shows the normalized radial distribution of the accelerated electrons, which show very different distribution patterns. The solid black line shows the radial distribution of the electrons in the antiparallel case, where electrons are concentrated near the optical axis ($r < 5$ μm). The dashed black line shows the distribution in the parallel case, where the electrons are distributed broadly off the axis. The result in Fig. 4, thus, presents that in the antiparallel case, the high-energy electrons are distributed along the optical axis.

In addition, the antiparallel CPLG laser pulse produces an electron bunch highly localized in the z coordinate. The solid red lines in Fig. 5a, b represent the electron densities along the optical axis (integrated over the xy plane for a given z) for the antiparallel and the parallel cases, respectively. In Fig. 5a, two electron bunches are identified. The first bunch is peaked at $z \approx 2.5$ μm and has a width of $\Delta z_{\mathrm{FWHM}} \approx 0.1$ μm, corresponding to $\Delta t_{\mathrm{FWHM}} \approx 0.3$ fs. The second broad bunch is found at $z \approx 1.5$ μm. The distance between the two bunches is about 1 μm, which is slightly longer than the laser wavelength. This is because the electrons in the second bunch have been detached from the first bunch but to be in the deceleration phase while having some momentum. After further acceleration owing to the strong longitudinal electric field formed in this region, the electrons gain more kinetic energy along with some divergence. Note that the most energetic electrons are in the second bunch around $z \approx 1.5$ μm, where the longitudinal electric field is most intense. This can be seen by looking at the electron distribution in the (r, z) plane together with their energy spectrum (color) in Fig. 5a. If a longer antiparallel CPLG laser pulse is used, a high-energy electron pulse train can be generated (see Fig. 7a). In the parallel case (Fig. 5b), the electrons are not bunched in the z coordinate and are more divergent, consistent with the beam pattern shown in Fig. 3b.

To accelerate electrons efficiently with the longitudinal electric field, electrons must be kept in the acceleration phase of the field. Since most acceleration occurs within the Rayleigh range [22], we define the acceleration time as $t_{\mathrm{acc}} = z_R/c$, where c is the speed of light. Additionally, we define the dephasing time t_{dep} as the time it takes for an electron to dephase from the acceleration phase of the longitudinal field. This transition occurs when the phase of the field, $\omega t - kz$, changes by π, leading to a transition from an accelerating force to a decelerating force for the electron. Therefore, we obtain the expression for the dephasing time as $\omega t_{\mathrm{dep}} - kz = \pi$. Then the dephasing time is $T_{\mathrm{laser}}\pi/2(1-\beta)$, where T_{laser} is the optical period of the laser, and β is the ratio of the velocity of electrons to the speed of light. Requiring $t_{\mathrm{dep}} > t_{\mathrm{acc}}$ gives the condition of $\beta > 0.965$, which corresponds to the relativistic Lorentz factor of $\gamma > 4$ in our case with the waist radius of $w_0 = 2$ μm. The acceleration of electrons by the longitudinal electric field of the antiparallel CPLG laser pulse is, thus, effective for $a_{z0} > 4$. Ideally, if the electrons are accelerated by the maximum longitudinal field within the Rayleigh range we can obtain ideal scaling in laser power as $E_{\mathrm{Max}}(\mathrm{MeV}) = eE_{z,\mathrm{Max}} z_R = 692\sqrt{P[PW]}$.

In Fig. 6, the energy scaling is examined by plotting the maximum kinetic energy of accelerated electrons in our simulations for different laser powers. The solid line in Fig. 6 represents the estimated scaling $E_{\mathrm{Max}}(\mathrm{MeV}) = 692\sqrt{P[PW]}$, and the dashed line does

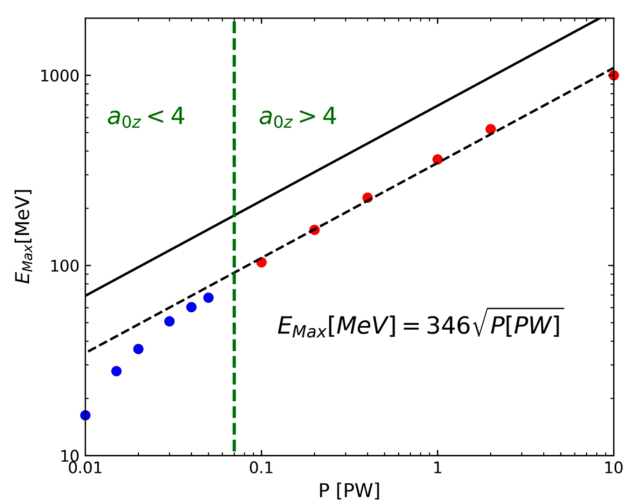

Fig. 6 Maximum electron energy in the simulation for different laser powers. The maximum electron energy is reached at the end of the simulation time, or at 600 fs. The solid black line shows the ideal scaling $E_{\mathrm{Max}}(\mathrm{MeV}) = 672\sqrt{P[PW]}$. The dashed black line shows 50% of the ideal scaling, $E_{\mathrm{Max}}(\mathrm{MeV}) = 346\sqrt{P[PW]}$. $a_{z0} = 4$ is indicated by a vertical dashed green line

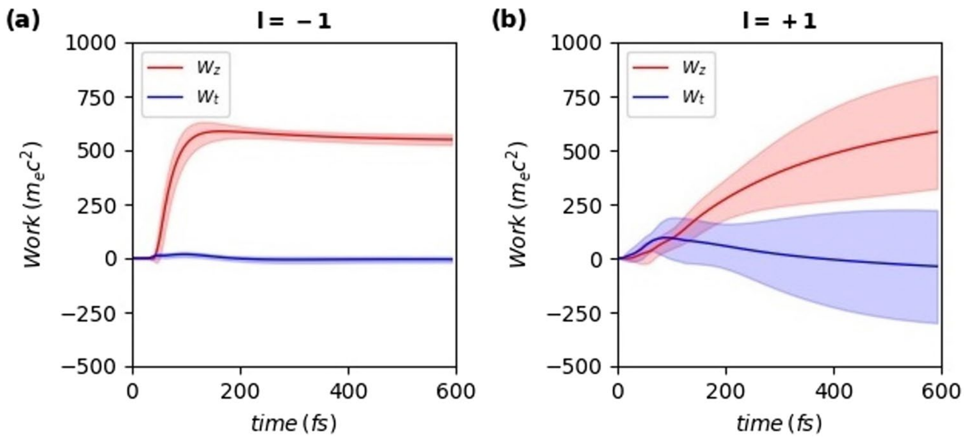

Fig. 7 **a** The amount of work done by the longitudinal electric field (W_z) and transverse electric field (W_t) for the antiparallel case. This figure shows the amount of work done by each field on 100 randomly selected electrons located in the dense region (z=2–3 μm) in Fig. 5a having an energy of 250–300 MeV. **b** A similar figure is drawn for the parallel case. This figure shows the amount of work done by each field on 100 randomly selected electrons located in the dense region (z=0–1 μm) in Fig. 5b having an energy of 250–300 MeV. The shaded region corresponds to the standard deviation of each value

that obtained from the PIC simulations with $a_{0z} > 4$, $E_{\text{Max}}(\text{MeV}) = 346\sqrt{P[PW]}$. The two scalings match each other well in the exponent of the laser power, albeit the absolute energy values from the simulation scaling are half of those from the estimated scaling. Such a reduced efficiency was also reported for the VLA with radially polarized laser pulses [22]. When we obtained the ideal scaling law for antiparallel CPLG laser pulses, we assumed that the electrons were accelerated along the optical axis. In practice, however, the accelerating electrons are pushed away from the optical axis owing to the ponderomotive force. This prevents them from experiencing the maximum acceleration field, leading to a deviation from the ideal scaling law. When $a_{z0} < 4$ (the vertical green dashed line marks the laser power for $a_{z0} = 4$), the maximum energy decreases further because the electrons cannot be kept in the acceleration phase of the longitudinal electric field, as discussed above. For parallel CPLG laser pulses, it is difficult to obtain the ideal scaling law by applying a similar method used for the antiparallel CPLG laser pulses. This is because the longitudinal field is nearly zero around the optical axis region in the parallel CPLG laser cases, which complicates the formulation of the ideal scaling law.

The ideal maximum energy scaling of the CPLG driven electron is about $\sqrt{2}$ times lower than that of electrons driven by the radially polarized laser pulses, $E_{\text{Max}}(\text{GeV}) = \sqrt{P[PW]}$ [42]. This is because the radially polarized laser mode, TM_{01}, is constructed by a combination of two antiparallel CPLG laser pulses,

$$E_z\left(TM_{01}\right) = \frac{1}{\sqrt{2}}\left(E_z(l=-1, s=+1) + E_z(l=+1, s=-1)\right), \tag{4}$$

which results in a $\sqrt{2}$ times larger longitudinal field strength. The beam divergence of the antiparallel CPLG accelerated electrons in Fig. 3a seems comparable to that of the electrons accelerated by a radially polarized laser pulse (=37 mrad) [25]. In short, the antiparallel CPLG laser pulse shows a comparable performance compared with the radially polarized laser pulse at a similar laser power. However, it is very challenging to produce radially polarized laser pulse at a PW level power. In contrast, it is much easier to produce high power CPLG laser pulses. In fact, a mirror-type phase plate has been developed recently as a practical way to produce ultra-intense CPLG laser pulses [32].

To determine which field plays a dominant role in the acceleration of electrons by the CPLG laser pulses, we examined the work done by the longitudinal electric field (W_z) and transverse electric field (W_t) on the electrons. Figure 7a shows the amount of work done on 100 randomly selected electrons by each field during the simulation time from 0 to 600 fs. The values of W_z and W_t are calculated as $-e\int_0^t \frac{E_z v_z}{m_e c^2}\mathrm{d}t$ and $-e\int_0^t \frac{E_x v_x + E_y v_y}{m_e c^2}\mathrm{d}t$, respectively. As shown in this Fig. 7a, the longitudinal field in the antiparallel case does much more work than the transverse field. This suggests that the electrons are predominantly accelerated by the longitudinal field. We note that the acceleration of electrons is also assisted by the longitudinal magnetic field as discussed in Refs. [36, 43]. The strong longitudinal magnetic field in the CPLG laser pulse trap electrons. This is because the longitudinal magnetic field can focus electrons toward the optic axis region since it has the same direction as the longitudinal electric field, as previously discussed in Ref. [43]. Therefore, the longitudinal magnetic field further increases the interaction time between the electrons and the

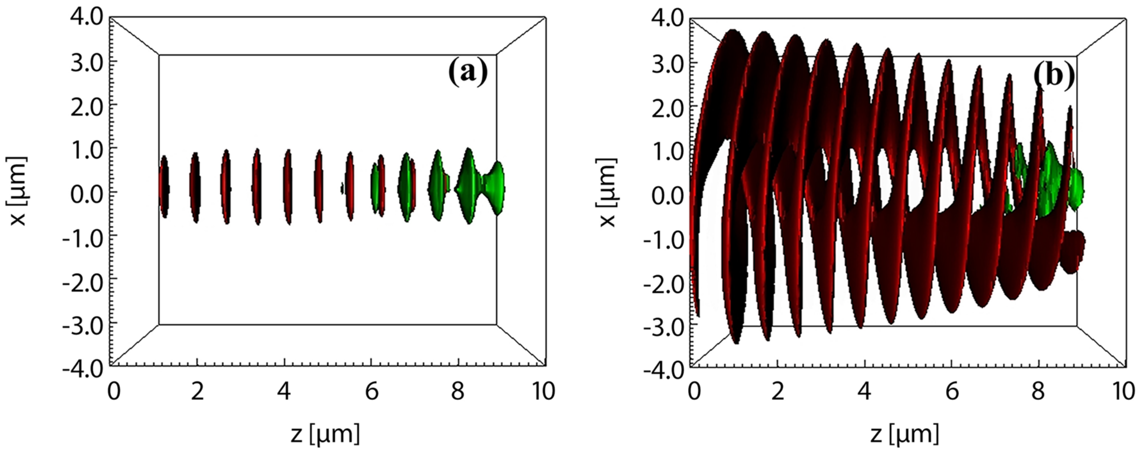

Fig. 8 Contour of electron density (green) and longitudinal electric field (red) for different values of l, **a** $l = -1$ and **b** $l = +1$. Polarization is fixed to the left circular polarization for all cases. A 2 PW, 30-fs-long laser pulse is used. The simulation time is 112 fs

longitudinal electric field. Figure 7b displays the amount of work received by 100 randomly chosen electrons during the simulation time from 0 to 600 fs. Compared with the antiparallel case, the amount of work done by the transverse field is no longer negligible, particularly during the initial interaction period ($t < 100$ fs), where W_t exceeds the value of W_z. After 100 fs, the effect of the longitudinal field on the electron acceleration process becomes dominant even in the parallel CPLG case. We confirm that the electrons are accelerated by both the transverse and the longitudinal fields in the parallel case.

In Fig. 8a, b, we show simulation results obtained with a 30 fs multi-cycle laser pulse. We have fixed the polarization of the laser as $s = +1$. The three-dimensional contour plots of the electron density is shown in green and the longitudinal electric field E_z is shown in red in Fig. 8a, b. The distribution of electrons closely matches the distribution of E_z in these figures. For instance, in Fig. 8(b), where $l = +1$, the E_z of the CPLG laser pulse has a twisting wavefront and the electrons show a similar distribution. When l is -1, the wavefront of the CPLG pulse is planar, and electrons form planar bunches as shown in Fig. 8a. Each electron bunch has a similar shape as that produced using a 5-fs laser pulse, and shows a pancake-like structure. Multiple electron bunches are produced, but less than the number of laser optical cycles. As discussed above, all electrons are accelerated by the strong electric field in the leading part of the laser pulse. Using electron injection method [42], one can even inject electrons at the desired optical cycle.

4 Conclusion

We have examined the effect of the longitudinal field on the acceleration of the electron beam from the CPLG laser pulse by comparing the electron beam quality generated from two different spin–orbit configurations, the so-called "parallel" and "antiparallel" cases. To examine the difference in electron beam quality by the configuration of l and s only, we simulated a simple setup using a few-cycle laser pulse and an low-density plasma target. In the antiparallel case, the longitudinal field is present inside the transverse field envelope with a planar wavefront resulting in collimated high-energy electrons, which is consistent with the predicted scaling law for field-induced acceleration that the maximum electron kinetic energy increases with the square root of incident laser power. We also found that the longitudinal field plays a significant role in the acceleration of electrons by the parallel CPLG laser pulse. While the transverse field envelopes of the parallel and antiparallel CPLG laser pulses were identical, indicating the same ponderomotive force on the electrons, the electron beam generated from the parallel CPLG laser pulse was more divergent and less energetic than that from the antiparallel CPLG laser pulse.

Our results demonstrate that the longitudinal field has a critical impact on the acceleration of the electron beam from the CPLG laser pulse, with a significantly different contribution of longitudinal and transverse fields observed between parallel and antiparallel configurations. For the first time, we have clearly shown that direct laser acceleration of electrons by antiparallel CPLG laser pulses is predominantly accomplished by the longitudinal field rather than by the ponderomotive force of the transverse field by comparing the case with parallel CPLG laser pulses. Moreover, we have demonstrated that both transverse and longitudinal fields impact the acceleration of electrons in parallel CPLG cases. These findings highlight the importance of considering the longitudinal field in the design and optimization of direct laser acceleration schemes. We anticipate that the difference in electron beam quality observed in our simulations can be confirmed experimentally.

Supplementary Information The online version contains supplementary material available at https://doi.org/10.1007/s00340-023-07996-y.

Acknowledgements This work was supported by Institute for Basic Science under IBS-R012-D1 and by the National Research Foundation of Korea (NRF) grant funded by the Korea government (MSIT) (No. 2023R1A2C1002912). W. B. was also supported by the GIST Research Project grant funded by the GIST in 2023. K. H. P. and C. M. K were supported by Ultrashort Quantum Beam Facility operation program (140011) through APRI, GIST and GIST Research Institute grant funded by the GIST in 2023.

Author contributions HS, CK, WB, and CN wrote the main manuscript text. HS, KP, JW, JS, SL, and CR performed the simulations and analyzed the data. All authors reviewed the manuscript.

Data availability The data that support the findings of this study are available from the corresponding author upon reasonable request.

Declarations

Conflict of interest The authors declare no conflict of interest.

References

1. T. Tajima, J.M. Dawson, Phys. Rev. Lett. **43**, 267 (1979)
2. S.C. Wilks, A.B. Langdon, T.E. Cowan, M. Roth, M. Singh, S. Hatchett, M.H. Key, D. Pennington, A. MacKinnon, R.A. Snavely, Phys. Plasmas **8**, 542 (2001)
3. A. Pukhov, J. Meyer-ter-Vehn, Appl. Phys. B **74**, 355 (2002)
4. J. Faure, Y. Glinec, A. Pukhov, S. Kiselev, S. Gordienko, E. Lefebvre, J.-P. Rousseau, F. Burgy, V. Malka, Nature **431**, 541 (2004)
5. C.G.R. Geddes, C. Toth, J. van Tilborg, E. Esarey, C.B. Schroeder, D. Bruhwiler, C. Nieter, J. Cary, W.P. Leemans, Nature **431**, 538 (2004)
6. S.P.D. Mangles, C.D. Murphy, Z. Najmudin, A.G.R. Thomas, J.L. Collier, A.E. Dangor, E.J. Divall, P.S. Foster, J.G. Gallacher, C.J. Hooker, D.A. Jaroszynski, A.J. Langley, W.B. Mori, P.A. Norreys, F.S. Tsung, R. Viskup, B.R. Walton, K. Krushelnick, Nature **431**, 535 (2004)
7. J.W. Yoon, J.W. Yoon, Y.G. Kim, Y.G. Kim, I.W. Choi, I.W. Choi, J.H. Sung, J.H. Sung, H.W. Lee, S.K. Lee, S.K. Lee, S.K. Lee, C.H. Nam, C.H. Nam, C.H. Nam, Optica **8**, 630 (2021)
8. H. Daido, M. Nishiuchi, A.S. Pirozhkov, Rep. Prog. Phys. **75**, 056401 (2012)
9. A. Macchi, *A Superintense Laser-Plasma Interaction Theory Primer* (Springer, New York, 2013)
10. S.D. Kraft, C. Richter, K. Zeil, M. Baumann, E. Beyreuther, S. Bock, M. Bussmann, T.E. Cowan, Y. Dammene, W. Enghardt, U. Helbig, L. Karsch, T. Kluge, L. Laschinsky, E. Lessmann, J. Metzkes, D. Naumburger, R. Sauerbrey, M. Schürer, M. Sobiella, J. Woithe, U. Schramm, J. Pawelke, New J. Phys. **12**, 085003 (2010)
11. C. Song, J. Won, J. Song, W. Bang, Int. Commun. Heat Mass Transf. **135**, 106070 (2022)
12. C. Song, S. Lee, W. Bang, Sci. Rep. **12**, 15173 (2022)
13. H. Song, C.M. Kim, J. Won, J. Song, S. Lee, C.-M. Ryu, W. Bang, C.H. Nam, Sci. Rep. **13**, 310 (2023)
14. A. Higginson, R.J. Gray, M. King, R.J. Dance, S.D.R. Williamson, N.M.H. Butler, R. Wilson, R. Capdessus, C. Armstrong, J.S. Green, S.J. Hawkes, P. Martin, W.Q. Wei, S.R. Mirfayzi, X.H. Yuan, S. Kar, M. Borghesi, R.J. Clarke, D. Neely, P. McKenna, Nat. Commun. **9**, 724 (2018)
15. F. Wagner, O. Deppert, C. Brabetz, P. Fiala, A. Kleinschmidt, P. Poth, V.A. Schanz, A. Tebartz, B. Zielbauer, M. Roth, T. Stöhlker, V. Bagnoud, Phys. Rev. Lett. **116**, 205002 (2016)
16. A.J. Gonsalves, K. Nakamura, J. Daniels, C. Benedetti, C. Pieronek, T.C.H. de Raadt, S. Steinke, J.H. Bin, S.S. Bulanov, J. van Tilborg, C.G.R. Geddes, C.B. Schroeder, C.S. Tóth, E. Esarey, K. Swanson, L. Fan-Chiang, G. Bagdasarov, N. Bobrova, V. Gasilov, G. Korn, P. Sasorov, W.P. Leemans, Phys. Rev. Lett. **122**, 084801 (2019)
17. W.P. Leemans, A.J. Gonsalves, H.-S. Mao, K. Nakamura, C. Benedetti, C.B. Schroeder, C.S. Tóth, J. Daniels, D.E. Mittelberger, S.S. Bulanov, J.-L. Vay, C.G.R. Geddes, E. Esarey, Phys. Rev. Lett. **113**, 245002 (2014)
18. H.T. Kim, K.H. Pae, H.J. Cha, I.J. Kim, T.J. Yu, J.H. Sung, S.K. Lee, T.M. Jeong, J. Lee, Phys. Rev. Lett. **111**, 165002 (2013)
19. H.T. Kim, V.B. Pathak, K.H. Pae, A. Lifschitz, F. Sylla, J.H. Shin, C. Hojbota, S.K. Lee, J.H. Sung, H.W. Lee, E. Guillaume, C. Thaury, K. Nakajima, J. Vieira, L.O. Silva, V. Malka, C.H. Nam, Sci. Rep. **7**, 10203 (2017)
20. M. Thévenet, A. Leblanc, S. Kahaly, H. Vincenti, A. Vernier, F. Quéré, J. Faure, Nat. Phys. (2015)
21. V. Marceau, C. Varin, T. Brabec, M. Piché, Phys. Rev. Lett. **111** (2013)
22. C. Varin, S. Payeur, V. Marceau, S. Fourmaux, A. April, B. Schmidt, P.-L. Fortin, N. Thiré, T. Brabec, F. Légaré, J.-C. Kieffer, M. Piché, Appl. Sci. **3**, 70 (2013)
23. L.J. Wong, K.-H. Hong, S. Carbajo, A. Fallahi, P. Piot, M. Soljačić, J.D. Joannopoulos, F.X. Kärtner, I. Kaminer, Sci. Rep. **7** (2017)
24. L. Fedeli, A. Sainte-Marie, N. Zaim, M. Thévenet, J.L. Vay, A. Myers, F. Quéré, H. Vincenti, Phys. Rev. Lett. **127**, 114801 (2021)
25. S. Payeur, S. Fourmaux, B.E. Schmidt, J.P. MacLean, C. Tchervenkov, F. Légaré, M. Piché, J.C. Kieffer, Appl. Phys. Lett. **101**, 041105 (2012)
26. R. Dorn, S. Quabis, G. Leuchs, Phys. Rev. Lett. **91**, 233901 (2003)
27. S. Carbajo, E. Granados, D. Schimpf, A. Sell, K.-H. Hong, J. Moses, F.X. Kärtner, Opt. Lett. **39**, 2487 (2014)
28. M. Wen, Y.I. Salamin, C.H. Keitel, Opt. Express OE **27**, 557 (2019)
29. M. Wen, Y.I. Salamin, C.H. Keitel, Phys. Rev. Appl. **13**, 034001 (2020)
30. Y. Cao, L.X. Hu, L.X. Hu, Y.T. Hu, J. Zhao, D.B. Zou, X.H. Yang, F.P. Zhang, F.Q. Shao, T.P. Yu, T.P. Yu, Opt. Express OE **29**, 30223 (2021)
31. Y. Zhao, D. Wang, R. Zhao, Y. Leng, Opt. Express **25**, 20866 (2017)
32. J.Y. Bae, C. Jeon, K.H. Pae, C.M. Kim, H.S. Kim, I. Han, W.-J. Yeo, B. Jeong, M. Jeon, D.-H. Lee, D.U. Kim, S. Hyun, H. Hur, K.-S. Lee, G.H. Kim, K.S. Chang, I.W. Choi, C.H. Nam, I.J. Kim, Results Phys. **19**, 103499 (2020)
33. L. Allen, M.W. Beijersbergen, R.J.C. Spreeuw, J.P. Woerdman, Phys. Rev. A **45**, 8185 (1992)
34. L.-X. Hu, T.-P. Yu, Z.-M. Sheng, J. Vieira, D.-B. Zou, Y. Yin, P. McKenna, F.-Q. Shao, Sci. Rep. **8**, 7282 (2018)
35. L.-X. Hu, T.-P. Yu, H.-Z. Li, Y. Yin, P. McKenna, F.-Q. Shao, Opt. Lett. **43**, 2615 (2018)
36. Y. Shi, D. Blackman, D. Stutman, A. Arefiev, Phys. Rev. Lett. **126**, 234801 (2021)
37. Y. Shi, D.R. Blackman, A. Arefiev, Plasma Phys. Control. Fusion **63**, 125032 (2021)
38. K.H. Pae, C.M. Kim, V.B. Pathak, C.-M. Ryu, C.H. Nam, Plasma Phys. Control. Fusion (2022)

39. T.D. Arber, K. Bennett, C.S. Brady, A. Lawrence-Douglas, M.G. Ramsay, N.J. Sircombe, P. Gillies, R.G. Evans, H. Schmitz, A.R. Bell, C.P. Ridgers, Plasma Phys. Control. Fusion **57**, 113001 (2015)
40. N. Zaïm, M. Thévenet, A. Lifschitz, J. Faure, Phys. Rev. Lett. **119**, 094801 (2017)
41. S. Carbajo, E.A. Nanni, L.J. Wong, G. Moriena, P.D. Keathley, G. Laurent, R.J.D. Miller, F.X. Kärtner, Phys. Rev. Accel. Beams **19**, 021303 (2016)
42. P.-L. Fortin, M. Piché, C. Varin, J. Phys. B **43**, 025401 (2010)
43. N. Milosevic, P.B. Corkum, T. Brabec, Phys. Rev. Lett. **92**, 013002 (2004)